
A Time-To-Frequency Converter for Measuring the Shape of Short Optical Pulses

Introduction

First noted in the 1960s, a mathematical equivalence exists between paraxial beam diffraction and dispersive pulse broadening.^{1–3} This equivalence, known as space–time duality, has led to the development of temporal analogs of several optical devices. An important component of such devices is the time lens,^{4,5} which is designed to impose a time-dependent parabolic phase across an optical pulse passing through it, just as a traditional lens provides a parabolic phase in space. The development of such a time lens has led to applications such as temporal imaging,^{4–7} spectral phase conjugation,⁷ and temporal cloaking.^{7,8}

Most modern time lenses produce the required parabolic phase using nonlinear effects such as four-wave mixing (FWM),^{7–10} which requires a highly nonlinear waveguide and careful control of the pump dispersion and timing. Using an electro-optic phase modulator driven by a phase-locked sinusoidal radio-frequency (rf) signal, we must adjust the timing of our test pulse within only one cycle of the rf signal, a task that can be accomplished with commercially available phase shifters. Additionally, the electro-optic phase shift does not have the intensity dependence of FWM and can be used for test pulses of any energy.^{11–16}

One of LLE’s diagnostic needs is to measure the shape of infrared ($\lambda = 1053\text{-nm}$) pulses with durations in the range of 1 to 30 ps. Pre-shot characterization of such short-pulse beams is important for preventing damage to the system. Optical streak cameras have been used at LLE for this purpose;^{17–19} however, several challenges to streak cameras limit their use. First, time-of-flight broadening occurs because of variations in the kinetic energy of the generated photoelectrons. These variations in kinetic energy lead to different electron velocities and, therefore, different amounts of time to reach the other end of the streak tube. For an infrared-sensitive Ag-O-Cs photocathode (designated S-1 photocathode) used in a streak camera, this leads to impulse responses of several picoseconds in width. Second, space-charge effects cause the electrons generated from short, intense pulses to repel each other. This produces broadening of the electron pulse in the drift region of the streak tube, which causes the measured pulse to be

longer.^{19–22} The space-charge effects can be reduced by using lower-power pulses, but lower powers lead to signal-to-noise issues. The combination of these two factors means that streak cameras are not particularly well suited to measuring pulses of durations <10 ps. Finally, and perhaps most importantly, recent experience at LLE has shown that current optical streak tubes based on S-1 photocathodes have such a limited lifetime that the long-term costs of operating such streak cameras are not realistic. Therefore, it would be beneficial to develop new diagnostic techniques as alternatives to the streak cameras.

Temporal imaging systems are of particular interest because they can be run in both single-shot and averaging modes without changing the aperture and resolution of the time lens.⁹ They are also well suited to imaging picosecond to tens-of-picosecond pulses.⁷ In particular, electro-optic phase modulators driven by GHz-rf signals can have apertures in the tens of picoseconds. As a proof of concept, we have developed a pulse-imaging system that uses an electro-optic phase modulator as a time lens in a time-to-frequency converter configuration. Our device maps the pulse shape onto the spectrum, allowing us to record the pulse shape with an optical spectrum analyzer. In the following sections, we address the design of our system, compare its performance to streak-camera and autocorrelator traces, and discuss how the system can be scaled up to cover a range of 1 to 30 ps.

Theory and System Design

We use a time lens in a time-to-frequency conversion system in which the input pulse first propagates inside an optical fiber before passing through the time lens.^{10,23,24} For a linear system, the electric field at the output of the dispersive medium of length L can be related to the input electric field in the frequency domain as²⁵

$$\tilde{E}_1(\omega) = \tilde{E}_0(\omega) \exp\left[\frac{i\beta_2 L}{2} (\omega - \omega_0)^2\right], \quad (1)$$

where $\tilde{E}_1(\omega)$ is the Fourier transform of the output electric field and the dispersion effects inside the fiber are included by

the second derivative, $\beta_2 = d^2\beta/d\omega^2$, of the modal propagation constant β at the central frequency ω_0 of the pulse spectrum. The parameter β_2 takes into account the group-velocity dispersion (GVD) and affects both the duration of the input pulse and its chirp. The pulse duration and chirp after the fiber are determined by the group-delay dispersion (GDD), given by $D_1 = \beta_2 L$.

When an electro-optic phase modulator driven by a sinusoidal voltage is used as a time lens, the phase shift applied to the pulse has the form

$$\Phi(t) = \phi_0 \cos(2\pi\nu_m t), \quad (2)$$

where ϕ_0 is the amplitude of the phase modulation and ν_m is frequency of the rf signal used to drive the modulator. The phase amplitude is determined by $\phi_0 = \pi V/V_\pi$, where V is the amplitude of the rf voltage used to drive the modulator and V_π is the voltage required for the modulator to produce a phase shift of π , a known quantity for commercial modulators. The electric field after the phase modulator is then related to the electric field at the output of the dispersive medium as

$$E_2(t) = E_1(t) \exp[-i\Phi(t)]. \quad (3)$$

In close analogy to the focal length of a traditional lens, a focal GDD is used to describe a time lens; it is defined as^{5,26}

$$D_f = [(2\pi\nu_m)^2 \phi_0]^{-1}. \quad (4)$$

For a time-to-frequency converter, the length of the dispersive medium is chosen such that the GDD of the medium, $D_1 = \beta_2 L$, is equal to the focal GDD of the time lens, D_f (Ref. 7). Therefore, the required length in our case is $L = D_f / \beta_2$. When this condition is satisfied, the output-pulse spectrum maps the temporal shape of the input pulse according to the scaling relation^{10,23}

$$t = D_f(\omega - \omega_0). \quad (5)$$

As with a traditional lens, it is useful to define a time aperture and temporal resolution for our time lens. The time aperture is the longest Gaussian pulse that can be imaged by our system without significant distortion of its measured full width at half maximum (FWHM) and has the form⁵

$$\Delta T = \frac{1}{2\pi\nu_m}. \quad (6)$$

The time resolution is the shortest FWHM pulse duration that can be generated by compressing a pulse that fits within the time lens aperture and is given by⁷

$$\delta t = \frac{4 \ln(2)}{2\pi\nu_m \phi_0}. \quad (7)$$

A schematic of the experimental setup is shown in Fig. 152.15. A mode-locked laser (High Q femtoTrian IC-1053-400 fs Yb) producing 150-fs pulses at 1053 nm with a 38-MHz

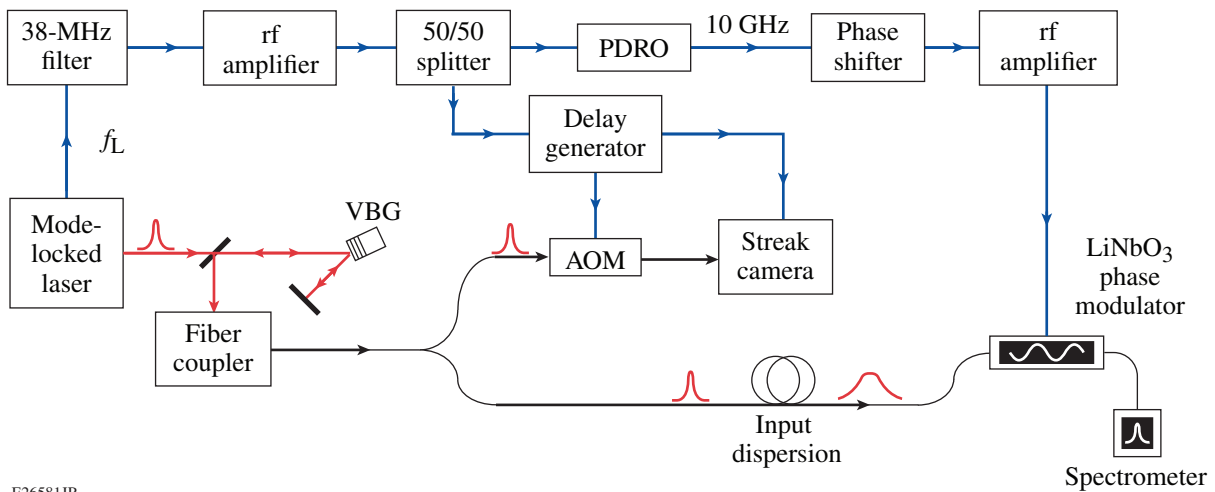


Figure 152.15 Experimental setup for a time-to-frequency converter using a phase modulator as a time lens and an optical fiber for the input dispersion. AOM: acousto-optic modulator; PDRO: phase-locked dielectric resonator oscillator; rf: radio frequency; VBG: volume Bragg grating.

repetition rate was used as the source of optical pulses. The time lens was implemented using a high-efficiency electro-optic phase modulator designed to operate at 800 nm but usable at 1053 nm (EOSPACE PM-5K4-10-PFU-PFU-800-LV-S). A fast photodiode (>100-MHz bandwidth) created an electronic signal of the laser pulse train, which was split into two parts with a 50/50 splitter. The first arm of the splitter was filtered with a 76-MHz bandpass filter to produce a synchronization signal at the second harmonic of the 38-MHz laser repetition rate. This 76-MHz signal matches the resonant frequency of a commercially available phase-locked dielectric resonator oscillator (PDRO), which uses phase locking to synchronize the pulse train to a high harmonic of the 76-MHz signal near 10 GHz (Ref. 27). The 10-GHz output was sent through a phase shifter, which allows one to adjust the timing between the 10-GHz signal and the pulse train so the time lens could be properly aligned. The resulting rf signal was amplified by a 33-dBm microwave amplifier and used to drive the phase modulator. This allowed our phase modulator to produce a sinusoidal phase modulation with a maximum phase amplitude of $\phi_0 = 16$ rad.

Using $\nu_m = 10$ GHz and a maximum phase amplitude of $\phi_0 = 16$ rad in Eqs. (6) and (7) gives a time aperture of $\Delta T = 15.9$ ps and a resolution of $\delta t = 2.75$ ps. The minimum focal dispersion for the time lens is then found using Eq. (4) to be $D_f = 15.8$ ps². To calibrate the time lens, the sinusoidal phase modulation is scanned across the pulse using a phase shifter and the amplitude of the rf voltage is adjusted until the peak of the pulse spectrum oscillates over a 1.2-nm range. To create the input GDD, a single-mode fiber (Corning HI1060) was used. Using the value of $\beta_2 = 23.8$ ps²/km at 1053 nm, 667 m of this fiber was required to give the input dispersion of $D_1 = 15.8$ ps². The chirped pulse was then sent through the phase modulator and the spectrum was recorded using an optical spectrum analyzer (Yokogawa AQ6370D).

Because the laser source produces pulses shorter than the resolution of the time lens, a spectral filter must be applied to the laser signal to broaden the pulse in time. A volume Bragg grating (VBG) with a 0.5-nm bandwidth was used to filter the spectrum. The VBG was used in a double-pass configuration to better attenuate the wings of the spectrum, resulting in a final spectral bandwidth of 0.254 nm.

The second arm of the rf line was filtered to 38 MHz and was used as a clock for a digital delay generator (Stanford Instruments DG645), which triggered an acousto-optic modulator (AOM) and a Rochester Optical Streak System (ROSS).¹⁷ The AOM was used to gate the pulse train to achieve a 0.1-Hz

repetition rate to prevent damage to the photocathode of the ROSS and to allow only a single pulse to be captured in the streak camera image, thereby eliminating jitter. The ROSS then captured images of the pulse shape, which were used as a comparison for the time-lens measurements.

Although the time lens has a theoretical aperture of 15.9 ps, this value was found, based on the FWHM of the measured pulse, to be largely the same as the FWHM of the actual pulse. However, even if pulses shorter than the time aperture are used, the wings of the pulse, which extend outside of the time aperture, can still see significant distortions. To explore this effect, numerical simulations of the pulse shape measured by a time-to-frequency converter with the same parameters as our experimental time lens were performed. The input dispersion and phase modulation were modeled using Eqs. (1) and (3), respectively. The frequency axis is scaled to the time axis using the relation given in Eq. (5).

Figure 152.16 shows the results for Gaussian input pulses with a FWHM of (a) 15 ps, (b) 12 ps, and (c) 10 ps. The pulse shape is plotted on a logarithmic scale to better show the behavior in the pulse wings. Comparing the three plots, it is shown that the 12-ps and 10-ps pulses in Figs. 152.16(b) and 152.16(c), respectively, are well imaged in the wings, while the 15-ps pulse has significant errors. Note that the wings are beginning to distort for the 12-ps pulse in Fig. 152.16(b), so the effective aperture is close to 12 ps. Also note that the FWHM of the 15-ps pulse is largely unchanged, with the errors arising from a suppression of the wings. A similar problem occurs for the time resolution, with the simulations showing that the resolution is closer to $\delta t = 3$ ps.

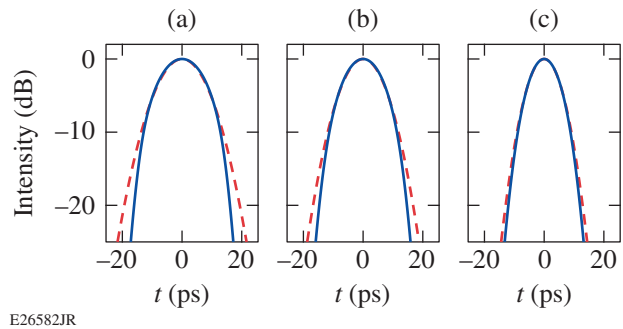
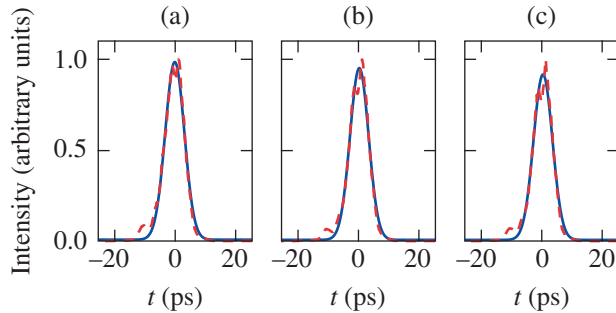


Figure 152.16 Numerical simulations showing the pulse shapes at the input (dashed red curve) and output (solid blue curve), respectively, of the time-to-frequency converter. Initial pulse widths are (a) $T_{\text{FWHM}} = 15$ ps, (b) $T_{\text{FWHM}} = 12$ ps, and (c) $T_{\text{FWHM}} = 10$ ps. The time axis for the output pulse was obtained using the scaling from Eq. (5).

Experimental Results

Three experimentally recorded spectra (dashed red curves) are shown in Fig. 152.17. The wavelength axis has been converted to a time axis by first converting wavelength to frequency and then using the focal GDD, $D_f = 15.8 \text{ ps}^2$, as a conversion factor to time. A Gaussian fit (solid blue curves) for each pulse provides a measure of the FWHM duration of the pulse. Our measurements show a typical pulse width of around 7.2 ps, with a few traces showing FWHM pulse durations near 7.32 ps, as in Fig. 152.17(a).

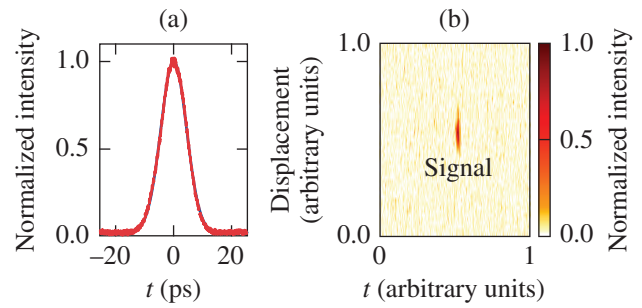


E26583JR

Figure 152.17

Measurement of the pulse shape produced by the volume Bragg grating using the time-to-frequency converter (dashed red curves) for (a) $T_{\text{FWHM}} = 7.32 \text{ ps}$, (b) $T_{\text{FWHM}} = 7.13 \text{ ps}$, and (c) $T_{\text{FWHM}} = 7.24 \text{ ps}$. The time axis is obtained using the scaling from Eq. (5). A Gaussian fit to the data is shown as the solid blue curves.

We first compare these measurements to an autocorrelation trace of the pulse as shown in Fig. 152.18(a). Because the autocorrelation signal was very weak as a result of the low peak intensity of our filtered pulses, the oscilloscope trace was averaged over 512 traces. The autocorrelation was then fitted with a Gaussian profile and found to have a FWHM duration of 10.31 ps. Using the known decorrelation factor of 0.707 for Gaussian pulses, a pulse width of $T_{\text{FWHM}} = 7.29 \text{ ps}$ was obtained, which agreed very well with the FWHM calculated from the time-lens measurements in Fig. 152.17 of $7.20 \pm 0.08 \text{ ps}$. To obtain this value, it was assumed that the input pulse shape was approximately Gaussian. While this was a good assumption in this case, the decorrelation factor can change drastically for different pulse shapes, taking a value of 0.65 for sech-shaped pulses. This is the reason why autocorrelation is not a useful technique for pulses of unknown shapes. For our time-lens technique, no assumptions are necessary for the pulse shape; as a result, it can be used for pulses of arbitrary shapes. Finally, the pulses measured by our time lens have a small asymmetric peak located near $t = -9 \text{ ps}$. This peak is likely caused by a secondary reflection in the VBG. It is not



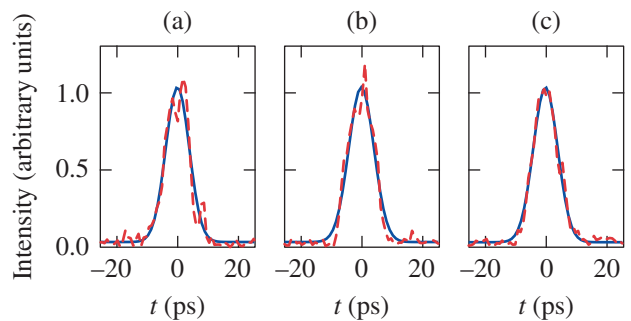
E26584JR

Figure 152.18

(a) Autocorrelation of pulses used to generate Fig. 152.17 has a width of $T_{\text{FWHM}} = 10.32 \text{ ps}$; (b) streak-camera image of the same pulses. The signal is labeled in the image.

present in the autocorrelation trace because autocorrelation involves the overlap of two copies of the same pulse, resulting in a symmetric trace. The ability of the time lens to measure asymmetries in the pulse shape is a major benefit of our technique over an autocorrelation-based technique.

Figure 152.18 compares these results to measurements from the ROSS. Figure 152.18(b) shows the image produced by the streak camera using the fastest sweep of 1.75 ns, where the region of the image corresponding to the signal pulse is zoomed in on. Each image is averaged along the displacement axis to produce a temporal profile for a single pulse. Figure 152.19 shows the resulting temporal profiles from three independent streak-camera traces, using 0.85 ps per pixel for the 1.75-ns sweep. After multiple shots, the pulse width measured on the streak camera was found to be $9.29 \pm 0.76 \text{ ps}$, which does not agree with the $7.20 \pm 0.08 \text{ ps}$ value deduced from the time-to-frequency converter. There are several reasons behind this discrepancy: First, the signal is inherently noisier compared



E26585JR

Figure 152.19

ROSS measurements of the pulse used to generate Fig. 152.17 (dashed red curves) and a Gaussian fit to the data (solid blue curves) for three different shots: (a) $T_{\text{FWHM}} = 9.01 \text{ ps}$, (b) $T_{\text{FWHM}} = 9.63 \text{ ps}$, and (c) $T_{\text{FWHM}} = 9.38 \text{ ps}$.

to the other two techniques owing to the single-shot nature of the streak camera. Second, the peak power of the pulses was considerably reduced to prevent the space-charge effects, which also decreased the signal-to-noise ratio. The primary reason the streak camera measurements are consistently over a picosecond longer than those found with either the time lens or the autocorrelator is related to the time-of-flight broadening. For an impulse response τ , the measured pulse width will be $T_m = \sqrt{T_0^2 + \tau^2}$. The measured impulse response of 5.78 ± 0.63 ps accounts for the observed discrepancy between the streak camera and the other two methods of measuring the pulse duration. Furthermore, even though the streak camera can potentially see the asymmetries in the pulse shape, the impulse response of the camera is longer than the asymmetry, which can no longer be resolved. Therefore, the same consistent bump in the pulse shape that could be clearly seen in the time-lens measurements is no longer seen.

Conclusions

A time-to-frequency converter using an electro-optic phase modulator acting as a time lens was built. Such a device was used to record the temporal shape of infrared pulses at a wavelength of 1053 nm (width of ~ 7 ps) and these measurements were compared to those made by using both a streak camera and an autocorrelator. Although the proof-of-concept system has successfully demonstrated the time-to-frequency conversion process, several improvements must be made before its use becomes practical. The most-challenging task is to expand the range of pulse durations that can be successfully imaged to cover the entire 1- to 30-ps range. As seen earlier, the current time lens can only accurately image pulses of less than 12 ps, so the time aperture must be expanded by lowering the drive frequency, ν_m . To reliably image the wings of 30-ps pulses, the drive frequency must be less than $\nu_m = 4$ GHz, with a time aperture of $\Delta T = 40$ ps.

By lowering the rf frequency, the time resolution will be expanded by the same factor according to Eq. (7). Therefore, the peak phase modulation must also increase by the same factor to maintain the same time resolution. However, it is also desired to lower the resolution from 3 ps to 1 ps, and the amplitude of the phase modulation must be increased to $\phi_0 = 120$ rad. The first step to accomplishing this will be to use a phase modulator designed for the 1053-nm wavelength. Such modulators can produce phase amplitudes of up to $\phi_0 = 30$ rad. If four of these modulators are connected in series, the required phase amplitude can be achieved. With the new frequency and amplitude for the time lens, the focal dispersion becomes $D_f = 13.2 \text{ ps}^2$, requiring only 554 m of single-mode fiber. This gives

a theoretical time resolution of 0.92 ps. However, numerical simulations show that the actual resolution of the time lens is closer to 2 ps. This is likely caused by the aperture of the time lens being smaller than predicted in Eq. (6). Therefore, the resolution will actually be larger than the predicted value according to Eq. (7). Indeed, a 2-ps pulse should be well imaged by this time lens. To image pulses with durations down to 1 ps, it would be necessary to double the total phase amplitude. This would require eight phase modulators connected in series, and the insertion losses would begin to affect the signal-to-noise ratio.

For the OMEGA EP Laser System in particular, this limitation can be worked around because the longer pulses are formed by chirping a shorter pulse with diffraction gratings. Because optical fiber has the opposite GVD as that of the diffraction gratings, the 30-ps pulse will actually recompress during propagation through the input fiber, allowing it to fit within the aperture of the time lens. The drive frequency can therefore be increased to $\nu_m = 7$ GHz to obtain a time aperture of $\Delta T = 21$ ps, while keeping the phase amplitude at $\phi_0 = 120$ rad. Using these parameters, our simulations show that the full 1- to 30-ps range can be well imaged with only slight errors for the 1-ps pulse. Therefore, we can image much longer pulses with a considerably weaker time lens if the long pulses are properly chirped.

Once the time-to-frequency converter is able to image the proper range of pulses, the system can be converted to a single-shot mode. This can be accomplished by feeding the output of the time lens into a single-shot spectrometer. For the above system with $\nu_m = 7$ GHz and $\phi_0 = 120$ rad, the spectrometer must be able to resolve spectral widths as small as 160 pm. Using a diffraction grating with a line density of 1200 g/mm and a charge-coupled device with 13.5- μm pixels, this resolution can be achieved with a spectrometer that is less than 30 cm long.

ACKNOWLEDGMENT

This material is based upon work supported by the Department of Energy National Nuclear Security Administration under Award Number DE-NA0001944, the University of Rochester, the New York State Energy Research and Development Authority, and the National Science Foundation under award ECCS-1505636.

REFERENCES

1. P. Tournois, C. R. Acad. Sci. **258**, 3839 (1964).
2. A. Papoulis, *Systems and Transforms with Applications in Optics* (McGraw-Hill, New York, 1968), p. 379.
3. S. A. Akhmanov, A. P. Sukhorukov, and A. S. Chirkin, Sov. Phys. JETP **28**, 748 (1969).

4. B. H. Kolner and M. Nazarathy, *Opt. Lett.* **14**, 630 (1989).
5. B. H. Kolner, *IEEE J. Quantum Electron.* **30**, 1951 (1994).
6. C. V. Bennett and B. Kolner, *IEEE J. Quantum Electron.* **36**, 430 (2000).
7. R. Salem, M. A. Foster, and A. L. Gaeta, *Adv. Opt. Photon.* **5**, 274 (2013).
8. M. Fridman *et al.*, *Nature* **481**, 62 (2012).
9. D. H. Broaddus *et al.*, *Opt. Express* **18**, 14,262 (2010).
10. A. Pasquazi *et al.*, *IEEE J. Sel. Top. Quantum Electron.* **18**, 629 (2012).
11. J. E. Bjorkholm, E. H. Turner, and D. B. Pearson, *Appl. Phys. Lett.* **26**, 564 (1975).
12. T. Kobayashi *et al.*, *IEEE J. Quantum Electron.* **24**, 382 (1988).
13. B. H. Kolner, *Appl. Phys. Lett.* **52**, 1122 (1988).
14. A. A. Godil, B. A. Auld, and D. M. Bloom, *Appl. Phys. Lett.* **62**, 1047 (1993).
15. M. T. Kauffman *et al.*, *Electron. Lett.* **29**, 268 (1993).
16. A. A. Godil, B. A. Auld, and D. M. Bloom, *IEEE J. Quantum Electron.* **30**, 827 (1994).
17. W. R. Donaldson, R. Boni, R. L. Keck, and P. A. Jaanimagi, *Rev. Sci. Instrum.* **73**, 2606 (2002).
18. R. A. Lerche, J. W. McDonald, R. L. Griffith, G. Vergel de Dios, D. S. Andrews, A. W. Huey, P. M. Bell, O. L. Landen, P. A. Jaanimagi, and R. Boni, *Rev. Sci. Instrum.* **75**, 4042 (2004).
19. J. Qiao, P. A. Jaanimagi, R. Boni, J. Bromage, and E. Hill, *Rev. Sci. Instrum.* **84**, 073104 (2013).
20. B.-L. Qian and H. E. Elsayed-Ali, *J. Appl. Phys.* **91**, 462 (2002).
21. B. J. Siwick *et al.*, *J. Appl. Phys.* **92**, 1643 (2002).
22. A. Verna *et al.*, *J. Electron. Spectrosc. Relat. Phenom.* **209**, 14 (2016).
23. M. T. Kauffman *et al.*, *Appl. Phys. Lett.* **64**, 270 (1994).
24. M. A. Foster, R. Salem, and A. L. Gaeta, *Opt. Photonics News* **22**, 29 (2011).
25. G. P. Agrawal, *Nonlinear Fiber Optics*, 5th ed. (Elsevier, Amsterdam, 2013).
26. B. H. Kolner, *J. Opt. Soc. Am. A* **11**, 3229 (1994).
27. I. Kang, C. Dorrer, and F. Quochi, *Opt. Lett.* **28**, 2264 (2003).